AIAA AVIATION Forum
12-16 June 2023, San Diego, CA and Online
AIAA AVIATION 2023 Forum

10.2514/6.2023-3358

Tonal noise measurements and simulations of an Over-The-Wing propeller

H.N.J. Dekker[1], H.H. Brouwer[2], J.C. Kok[3], M. Laban[4] and M. Tuinstra[5]
Royal Netherlands Aerospace Centre, Marknesse, Flevoland, 8316 PR, The Netherlands

The aeroacoustic installation effects of an Over-The-Wing propeller are investigated through experiments and three different simulation techniques with an increasing degree of wing-propeller coupling. The most primitive simulation considers an isolated propeller in the non-uniform inflow imposed by the wing, in which loads are computed by a BEMT formulation with corrections for the unsteady components of lift and drag. Secondly, an iterative chain is developed where the inflow field to the propeller is obtained using a steady-RANS formulation with the inclusion of an actuator disk, combined with a lifting ling formulation. Finally, high-fidelity simulations are performed which make use of an unsteady-RANS formulation, with the propeller advancing in small azimuthal steps. The experiments and simulations show an effective reduction of the first BPF by noise shielding on the pressure side, while the noise increases on the opposite side of the wing. Trends in propulsive and acoustic performance are captured in the simulations, but discrepancies between predicted and measured values are present.

I. Nomenclature

B	=	number of blades
BPF	=	Blade Passing Frequency
C	=	wing chord
c_l	=	two-dimensional lift coefficient
c_p	=	two-dimensional pressure coefficient
C_{pow}	=	power coefficient
C_T	=	thrust coefficient
CNC	=	Computer Numerical Control
D	=	propeller diameter
dC_{pow}	=	delta power coefficient
dC_T	=	delta thrust coefficient
$dSPL$	=	delta Sound Pressure Level
G	=	Green's function
J	=	propeller advance ratio
k	=	wavenumber
p	=	total acoustic pressure field amplitude
P_f	=	propeller acoustic pressure field amplitude
$\hat{p}$	=	Fourrier transformed pressure
Q	=	propeller torque
R	=	propeller radius
Re_c	=	chord-based Reynolds number

[1] Ph.D. Candidate, Vertical Flight and Aeroacoustics Department; h.n.j.dekker-1@tudelft.nl. Member AIAA
[2] Senior Scientist, Vertical Flight and Aeroacoustics Department; harry.brouwer@nlr.nl
[3] Senior Scientist, Flight Physics and Loads Department; johan.kok@nlr.nl
[4] Senior Scientist, Flight Physics and Loads Department; martin.laban@nlr.nl
[5] Scientist Principal Aeroacoustics, Vertical Flight and Aeroacoustics Department; marthijn.tuinstra@nlr.nl. Member AIAA.

SPL	=	Sound Pressure Level
T	=	propeller thrust
V_∞	=	free-stream velocity
x_p	=	propeller x-position
y_p	=	propeller y-position
α	=	free-stream angle of attack
Ω	=	shaft frequency
∂S	=	boundary of wing section
$\partial \Omega$	=	boundary surface of scattering body

II. Introduction

Electrification of the propulsion system is of great interest to reduce the emissions of future aircraft [1]. The great scalability characteristics of electric motors has typically led to a tighter integration of the propulsors (propellers or fans) with the aerodynamic surfaces of the aircraft [2]. This is ultimately done to create beneficial coupling effect to increase aeropropulsive efficiency, resulting in a wide range of design solutions [3]. However, this often results in unexplored aerodynamic and aeroacoustic installation effects.

An example of such an integrated propulsion configuration is the Over-The-Wing-propeller [7] or Over-The-Wing distributed electric propulsion [4,8]. In this layout, the propulsors are positioned over the suction side of the wing, see Figure 1a. Using the suction upstream of the propeller, the dynamic pressure over the wing is reduced, leading to improved aerodynamic characteristics. A lift increase of 8% for the OTW propeller has been shown compared to an isolated wing [14]. This lift increase has shown to be sensitive to the chordwise position of the propeller, in which a propeller closer to the trailing edge gave the largest effect on the lift production [4].

Aside from the aerodynamic benefit, favorable effects to the acoustic signature of this propulsion system lay out are also expected. This comes in the form of shielding of the propeller noise by the wing's surface, which could be used to reduce fly-over noise [5].

While the shielding and lift enhancement characteristics provide a clear benefit compared to an isolated propeller-wing system, the effects of the wing on the propulsive efficiency are adverse. The wing's circulation alters the inflow conditions towards the propeller, as is illustrated in Figure 1b, resulting in an increase in flow velocity compared to the free-stream. As a consequence, propulsive efficiency losses of up to 16% have been noted [6]. Additionally, the wing imposes a stronger acceleration of the flow closer to its surface. This results in a non-uniform inflow condition to the propeller as illustrated in Figure 1b, causing periodic variations in blade loading. Unsteady loading is known to be a strong contribution to the aeroacoustic signature of propeller systems [17] and could cancel out the favorable shielding effect.

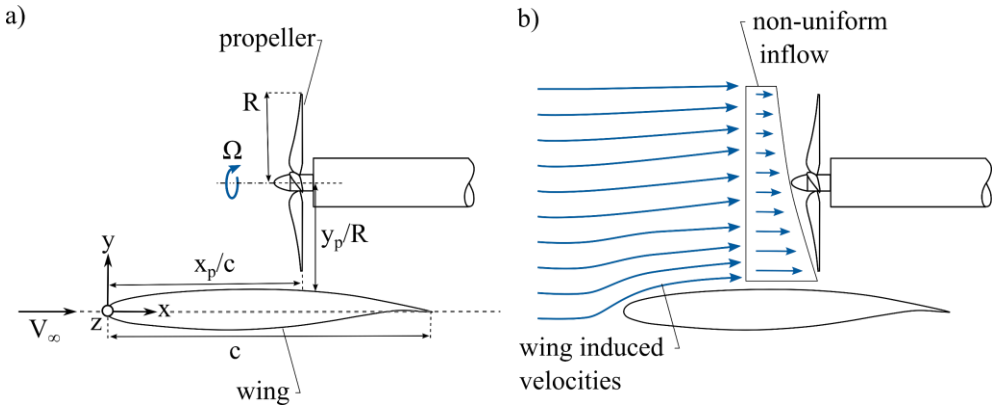

Figure 1 a) Schematic representation of the Over-The-Wing propeller with relevant parameters and system of coordinates and b) non-uniform inflow

Studies which investigate the aeroacoustic installation effects of the OTW-propeller in detail are currently not present in literature. Considering that the flow field is viscous, three-dimensional and unsteady, experimental measurements and high-fidelity simulations are required to investigate and assess both the noise reduction by shielding and the contribution by unsteady loading. When these installations effects are understood correctly, design guidelines can be formulated which make use of the beneficial and mitigate the detrimental installation effects.

The use of a low-fidelity tool allows for an efficient optimization of the propulsion system by varying the relative position of the propeller compared to the wing, and is therefore particularly useful when formulating these design guidelines. Current low-fidelity tools are typically designed for isolated propellers and therefore do not take the non-uniform inflow into account. Furthermore, the propeller will be positioned close to reflecting and scattering surfaces which will impact the acoustic profile of the system.

The objective of the current investigation is twofold. First of all, the aeroacoustic installation effects of the OTW propeller system are investigated. Here, the focus will be how the amplification of noise by unsteady loading compares to the favorable shielding effect. The investigation will be performed by using experimental data and results from three different simulation technique, which consider increasing degree of propeller-wing coupling and computational costs. Comparing the results of the different simulations with the experiments is the second objective of the study. This will provide information on the accuracy and suitability of low-fidelity tools for the trend analysis of this propulsion system.

The outline of the paper is as follows. In chapter III, the formulation of the simulation techniques are introduced. The experimental setup is then introduced in chapter IV. In chapter V, the installed propeller's performance trends and flow field results are presented.

III. Simulation Techniques

The three different simulation techniques are presented in this chapter, which are ranked by their relative degree of propeller-wing coupling. In the most straightforward approach, an isolated propeller in the non-uniform inflow imposed by the isolated wing is considered, effectively decoupling the propeller from wing system. As a second simulation technique, iterative coupling between the propeller and wing induced flow fields are included. For this a loop is created which consists of a lifting line simulation tool for isolated propellers and a steady RANS simulation with the inclusion of an actuator disk. Additionally, a Boundary Element Method has been implemented to account for the scattering and reflective surface of the wing. Finally, high-fidelity simulations are performed by means of an unsteady-RANS formulation with the propeller advancing in azimuthal steps. In this way there is a continuous coupling between propeller and wing-induced flow field. This simulation also includes the propeller sting and wind tunnel walls as used in the experiments. The different techniques are sketched schematically in Figure 2 and will be discussed in detail in this chapter.

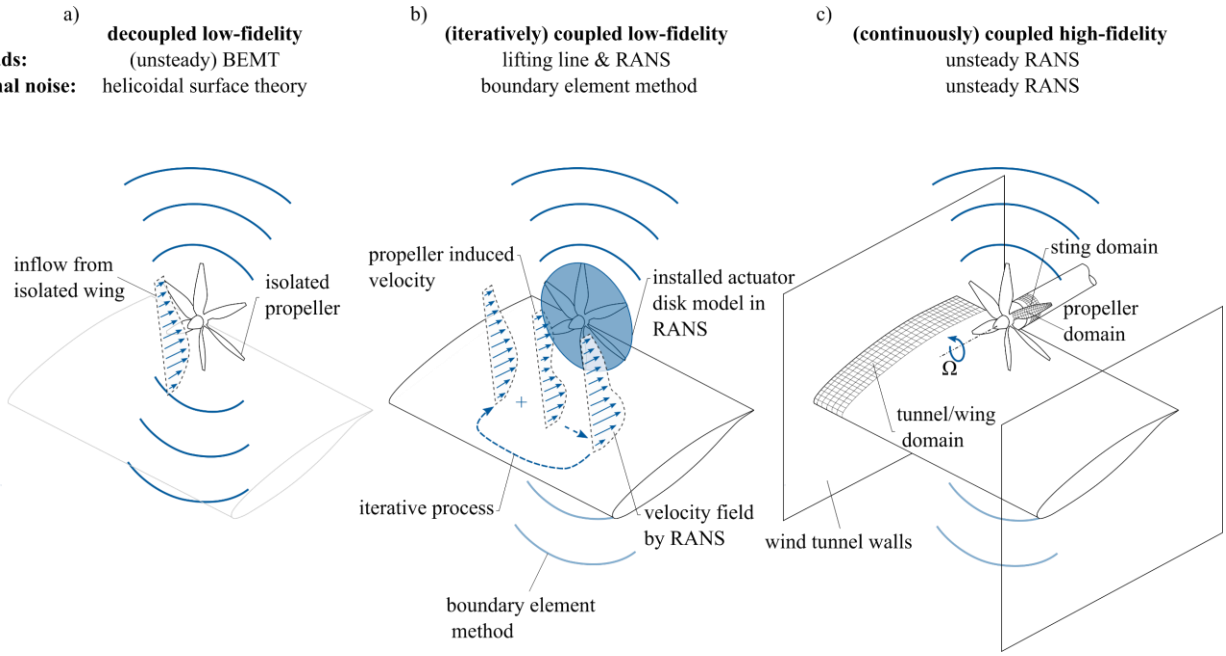

Figure 2 Different simulation techniques : a) isolated propeller in non-uniform and non-axial inflow, b) iterative chain and BEM to include the presence of the wing and c) high-fidelity unsteady RANS

A. Decoupled Low-Fidelity (BEMT)

The decoupled low-fidelity tool requires the flow field from the isolated wing as an input, see Figure 2a. This can be computed with relative ease with a potential flow solver. Nonetheless, the current version makes use of velocity field measurements around the isolated wing, resulting in a similar inflow field for the propeller. Then, for each azimuthal position of the blade in the non-uniform flow field, the loading of the blade is computed using Blade Element Momentum Theory (BEMT) in a quasi-steady manner. Then, by following a similar approach as [12], a correction for unsteady lift and drag effects is applied, by usage of the Sears function [13].

The information on the blade loading is used as an input to the helicoidal surface theory developed by Hanson [14] in which unsteady loading effects are accounted for [15]. In the simulation, a parabolic lift distribution over the blade section chord is assumed. Lift and drag are modelled as unsteady sources in the frequency domain. The propeller's thickness noise is modelled as an additional noise source. Considering the limited effect by the non-uniform inflow on the blade's tip Mach number for low-speed propellers, this noise source is considered to be steady along the blade's azimuth.

B. Coupled Low-Fidelity (LL+RANS)

For the coupled low fidelity simulation as illustrated in Figure 2b, use is made of a lifting-line method for propellers [9], combined with a RANS computation. The simulation starts with the computation of the forces on the isolated propeller in a uniform flow. Next, these forces are represented by an actuator disc which is placed above the wing, for a steady RANS computation of the flow field. This non-uniform flow field is then used as input for the computation of the unsteady forces on the blades, by using an adapted lifting-line model [10]. It should be noted that in this model the velocity induced by the unsteady component of the lift is neglected. The forces on the blades, which now vary with the azimuth, are then represented again by the actuator disc, and a new RANS computation is carried out. This cycle is repeated until convergence is reached, usually after only 3 iterations. At this stage the performance of the propeller is known, within the lifting-line approximation.

The acoustic pressure field is then computed for the isolated propeller with the converged unsteady forces acting on it. The effect of the wing on the acoustic field is computed by application of a simplified Boundary Element Method (BEM), currently without incorporation of the flow. The BEM equation for a tone with time dependency $e^{i\omega t}$ reads:

$$C(\vec{x})p(\vec{x}) = p_f(\vec{x}) + \int_{\partial\Omega} p(\vec{\xi}) \frac{\partial G(\vec{x};\vec{\xi})}{\partial \boldsymbol{n}} \mathrm{d}S_\xi \tag{1}$$

with p the amplitude of the total acoustic pressure field, p_f the field of the isolated propeller, and $\partial\Omega$ is the boundary surface of the scattering body. C equals ½ if $\vec{x}$ is on $\partial\Omega$, and equals 1 elsewhere. G is the Green's function for the Helmholtz operator in the free field. The next step is to solve this equation for $\vec{x} \in \partial\Omega$. To reduce complexity and computation time, it is assumed that the wing has a constant profile and is of infinite span. This allows Fourier transformation from the spanwise coordinate y to the wavenumber in this direction, denoted by α, which results into the following equation for the pressure on the surface:

$$\frac{1}{2}\hat{p}(x,\alpha,z) = \hat{p}_f(x,\alpha,z) + \int_{\partial S} \hat{p}(\xi,\alpha,\zeta) \frac{\partial \hat{G}_2(\alpha)}{\partial \boldsymbol{n}} ds \tag{2}$$

with $\hat{p}$ the Fourier transformed pressure and ∂S the 2D boundary of the wing section. $\hat{G}_2$ is the Green's function of the 2D Helmholtz operator:

$$\hat{G}_2(\alpha) = \frac{i}{4} H_0^{(2)}(\gamma r) \tag{3}$$

where $r = \sqrt{(x-\xi)^2 + (z-\zeta)^2}$, $\gamma = \sqrt{k^2 - \alpha^2}$, and k is the wavenumber ω/c. After discretization eq.(2) forms a matrix equation in 2 dimensions for each value of α, which can be readily solved by matrix inversion. Back-transformation from α to y yields the solution on the surface of the wing. The acoustic pressure at any point in the field can now be computed by simple numerical integration in eq.(1).

C. High-fidelity (URANS)

The high-fidelity simulations consist of URANS computations using NLR's in-house flow solver ENSOLV. This solver is based on multi-block structured grids, with the option to use Chimera (a.k.a. overset) grids. The RANS

equations are discretized in space by a fourth-order finite-volume scheme with low numerical dispersion and dissipation [11], to capture the propagation of acoustic waves accurately, and integrated in time by the second-order backward scheme. A grid has been generated that should be fine enough to capture not only the sound generation by the propeller but also the sound propagation inside the wind tunnel (up to 3 BPF). It consists of three overlapping Chimera domains (see Figure 2c): the propeller domain (14.4 M cells), the propeller hub and sting domain (43.5 M cells), and either the empty tunnel domain (isolated; 39.8 M cells) or the tunnel plus wing domain (installed; 56.0 M cells). The tunnel walls are included as slip boundaries. Near the tunnel walls, buffer zones are used that damp the acoustic waves in order to prevent reflections at the tunnel walls (to be consistent with the experimental set-up using acoustic transparent walls).

IV. Experimental Setup

A. Wind tunnel

The experiments were performed in the Aeroacoustic Wind Tunnel Facility at the Netherlands Aerospace Centre in Marknesse, see Figure 3. The facility consists of an anechoic chamber (9 x 8 x 6 m), yielding an absorption rate of 99% above 200Hz. To increase the quality of the aerodynamic measurements, a closed test section was used. This test section limits the turbulence intensity to a maximum of 0.01% at a free-stream velocity of 20 m/s. In order to mitigate any reflections of acoustic waves, the test section was fitted with acoustic transparent walls.

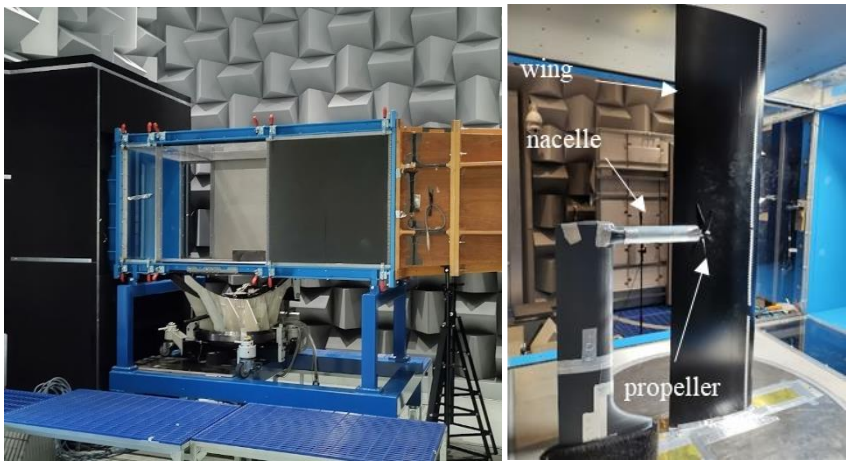

Figure 3 a) Exterior of the test section in the AWT, b) F15 wing model and nacelle with the propeller in the test section b). Note that one wall has been removed when taking these images.

B. Propeller and wing model

A F15 wing model was mounted vertically on a turntable in the floor of the closed test section, as shown in Figure 2. The chord of the wing comprises 240mm and the boundary layer was tripped at 10% chord on both the suction and pressure side. Over the suction side of the wing, a nacelle was positioned and connected to the same turntable as the wing, with its axis aligned with the wing's chord direction. Inside the nacelle, a brushless in runner motor is connected through a thrust (FUTEK LSB205) and torque sensor (FUTEK QTA141). The motor drives a custom design six-bladed propeller (radius of 63.5 mm) at a shaft frequency of 383 *Hz*. The experimental conditions are summarized in Table 1.

C. Aeroacoustic measurements

Acoustic measurements were performed to both measure the increase in noise of the propeller and to quantify the effect of noise shielding. The noise of the propeller is measured using a microphone array consisting of 64 microphones, see Figure 4. The array is positioned outside the test section at a distance of 0.70 m and aimed towards the suction side of the wing.

Additionally three free-field microphones are positioned outside of the test section on the pressure side of the wing to investigate the potential of noise shielding by the wing. The free-field microphones are positioned at a distance of

2.12 m from the center of the test section. All microphones are sampled at a frequency of 41 kHz for a time duration of 20 s for each data point.

Table 1 Over-The-Wing propeller system operating conditions

Wing chord c (mm)	240
Chord Reynolds number Re_c	240,000 – 480,000
Shaft frequency (Hz)	383
Blade Passing Frequency BPF (Hz)	2300
Number of blades B	6
Propeller radius R_1 (mm)	63.5
Propeller tip gap y_p/R_1	0.27
Propeller chord position x_p/c	0.6
Propeller advance ratio J	[0, 0.3, 0.45, 0.6]
Angle of attack α	0

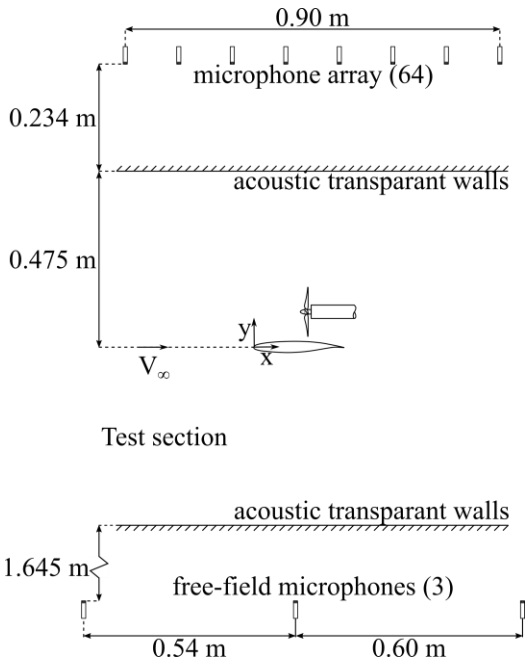

Figure 4 Schematic of top view of the anechoic room with microphone positions

D. Stereoscopic Particle Image Velocimetry

The inflow of the propeller is characterized in the (x,y)-plane (see Figure 1) using stereo-Particle Image Velocimetry (sPIV). For this, the acoustic transparent walls are replaced by optical transparent walls. The flow is seeded with DEHS tracer particles which are illuminated by an evergreen laser at a rate of 15 Hz. Recording is performed by two sCMOS cameras (*Imager sCMOS CLHS*) placed outside the section at a distance of 0.6 m from the center of the measurement region. The resulting field of view spans 19 x 25 cm^2 (3 R x 4 R). Each measurement comprises at least 300 recordings for a time duration of 20 s. The propeller is traversed, in steps of 10 mm to a maximum displacement of 50 mm (0.8 R) in both positive and negative z-direction. This allows for a 3C3D reconstruction of the time-averaged velocity field. An overview of the measurement parameters is presented in Table 2.

Table 2 Illumination and imaging conditions

Seeding type	DEHS
Illumination	Evergreen (200 mJ/pulse)
Sheet thickness *dz* (mm)	3
Repetition rate (Hz)	15
Camera type	2 x Imager sCMOS CLHS
Camera resolution	2560 x 2160 px^2
Stereo angle	35º
Objective focal length *f* (mm)	50
Numerical Aperture $f_\#$	8
Optical magnification *M*	0.009
Field of view (cm^2)	19 x 25
Number of recordings	300
Image analysis	Cross-correlation (32 x 32 px^2)
Vector pitch (mm)	0.6

V. Results

A. Isolated propeller loads

To validate the simulations, loading results for the isolated propeller are compared with the experimental measurements in Figure 5. The performance curves of C_T and C_{pow} show a parabolic relation with the advance ratio *J*. At an advance ratio of $J = 0.75$, the propeller is close to the windmilling state and provides a limited amount of thrust. The relative error of the simulations with the experimental data is given in the bottom half of Figure 5. The BEMT results show good agreement for thrust data of the isolated propeller, with errors below 3% for most of the conditions. Errors for the lifting line method are higher, caused by some discrepancy between the measured and simulated C_T-*J* trends. For the URANS results, only a single condition is known, for $J = 0.6$, which gives a relative error 13%. The large error for the URANS results is caused by the fact that the propeller is simulated in a fully turbulent environment, while in the experiments a laminar boundary layer is expected over a major part of the blades.

B. Tonal & Broadband noise

The simulations are limited to tonal noise, while broadband noise is also generated by the propeller. To compare the two contributions, noise spectra from the experimental data are computed from the center microphone positioned at the suction side (positive *y* in Figure 4). The tonal and broadband noise is split by performing "phased-locked" Fourrier transform [18] which are averaged over a large amount (≈7500) shaft revolution. Results for the installed configuration for $J = 0.3$ and $J = 0.6$ are given in Figure 6.

For the case of $J = 0.3$ in the top part of Figure 6 there is a broadband noise floor between 50 and 60 dB, while the first BPF is approximately 72 dB. Multitudes of the BPFs do not exceed the broadband noise, with the exception of the third BPF. When increasing the advance ratio to $J = 0.6$ in the bottom part of Figure 6, the broadband noise is increased over all frequencies, while the tonal noise is decreased by a reduction in blade loading.

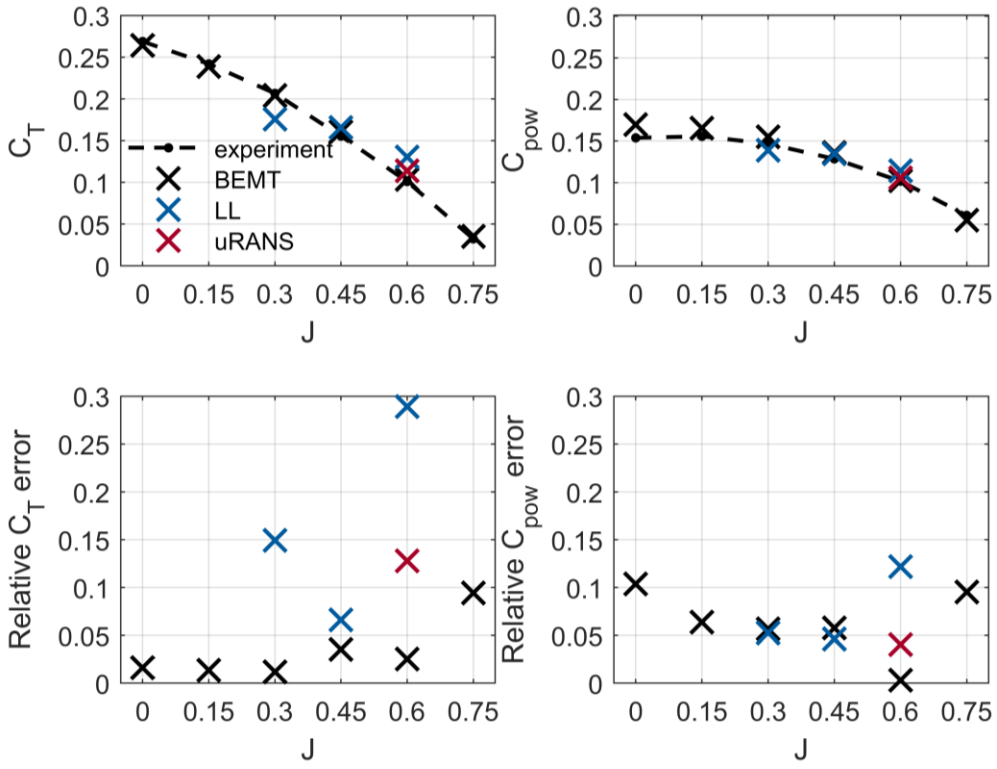

Figure 5 (Top) Isolated propeller thrust C_T (left) and power coefficient C_{pow} (right) as measured in the experiment and computed using the models for increasing advance ratio. (Bottom) Relative error between the simulations and the experiments.

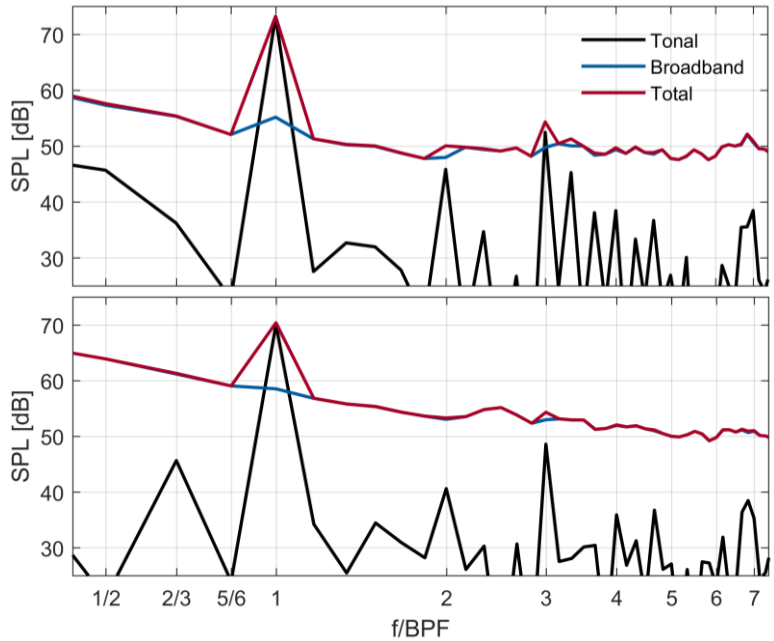

Figure 6 Acoustic spectra from the suction side microphone in the propeller plane for the installed propeller for J = 0.3 (top) and J = 0.6 (bottom).

The relative contribution of tonal and broadband noise can be compared by integration of the spectra of Figure 6. The results of which are given in Figure 7 as a function of the advance ratio J. From this follows the expected decrease in tonal noise with advance ratio. Nonetheless, the broadband noise follows a distinct shape. A relatively large amount of broadband noise is seen for $J = 0$ which is caused by laminar separation over the propeller blades. Furthermore, after $J = 0.3$, the broadband noise increases with J. This causes the broadband noise to be dominant for the $J = 0$ and $J = 0.6$.

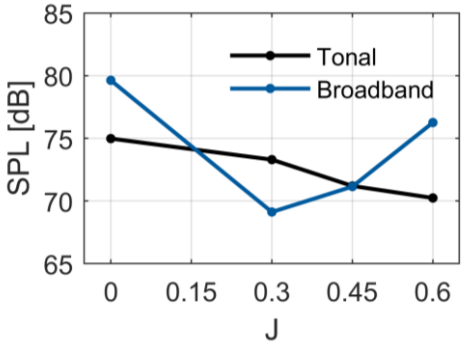

Figure 7 Integrated tonal and broadband spectra at the suction side of the installed propeller, as a function of advance ratio *J*

C. Inflow velocity field

The wing alters the inflow conditions to the propeller. For the iterative low-fidelity simulation, this effect is computed using a steady-RANS simulation with the inclusion of an actuator disk. This input for the low-fidelity simulation can be validated using the experimental PIV measurements. The measured velocity magnitude distribution for $J = 0.3$ (top) and $J = 0.6$ (bottom) in the plane through the propeller axis ($z = 0$) presented in Figure 8.

In Figure 9, the non-uniform inflow distribution by the wing's circulation is clearly visible from the experimental data; higher momentum is found between the propeller shaft and wing (negative y_p) compared to the upper part of the propeller inflow (positive y_p) for $J = 0.3$ (top left) and $J = 0.6$ (bottom left). Furthermore, in the high thrust conditions of $J = 0.3$ (top left), there appears a small region of flow separation between the propeller tip and wing surface, caused by the adverse pressure gradient induced by the propeller.

The velocity field as computed through the steady RANS formulation (right half of Figure 9) shows good agreement with the experimental flow field. Here, the separation of the slipstream with the wing's surface is also visible for $J = 0.3$ (top right). Propeller induced velocities upstream of the disk are slightly higher for the RANS results compared to the experimental data.

Since the propeller is traversed in the experimental measurements, a time-averaged 2D inflow plane (in (z,y)-coordinates) can be created, as presented Figure 9. From this it becomes apparent that inflow velocities are also not symmetric along the (y,z)-plane (i.e. spanwise variations). Higher velocities are found in positive z_p compared to negative z_p, which further contributes to the unsteady loading of the blades for the installed propeller. A similar inflow pattern is found for the results of the steady RANS simulation, in the right half of Figure 9.

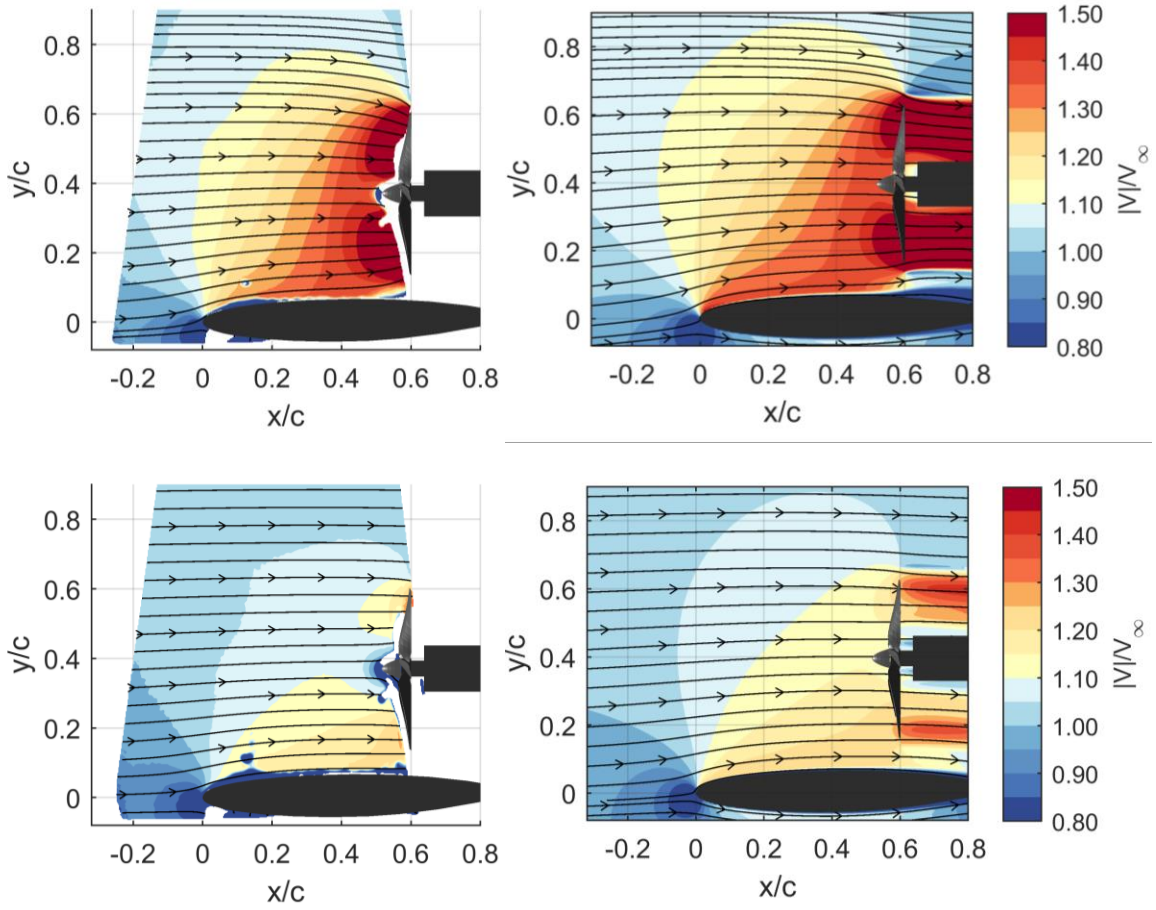

Figure 8 Time-averaged normalized velocity magnitude and 2D velocity streamlines in the (*x*,*y*)-plane for *J* = 0.3 (top) and *J* = 0.6 (bottom). The left side includes the experimental results while the RANS with inclusion of the actuator disk are given on the right.

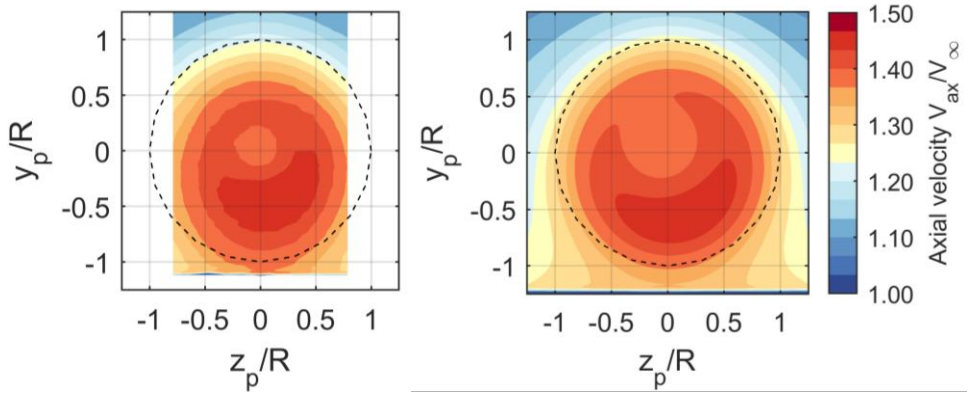

Figure 9 Experimental (left) and RANS (right) time-averaged normalized velocity magnitude in the (*z*,*y*)-plane at *x/c* = 0.5 for *J* = 0.3.

D. Propeller loading trends

Installed propeller performance is computed relative to the isolated propeller performance (i.e. $dC_T = C_{T,installed} - C_{T,isolated}$). Experimental data for the thrust and torque sensors, is compared to the integral loading of the simulations in Figure 10. In each condition, a thrust deficit is found for the installed propeller, compared to the isolated configuration. This thrust deficit is shown to increase with increasing advance ratio J, but is minimized for J = 0.3. All simulations show a reduction of thrust, although it is slightly under-predicted and the trend is more linear compared to the experiments.

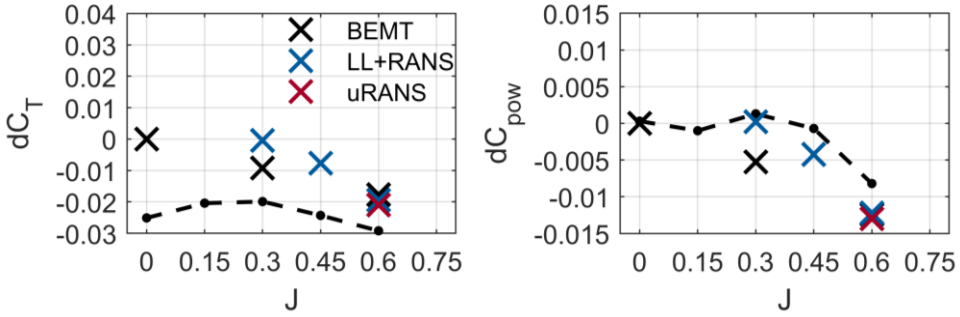

Figure 10 a) Propeller delta thrust coefficient dC_T and b) propeller delta power coefficient dC_{pow} as a function of the advance ratio J

The delta of the power coefficients dC_{pow} is computed in a similar way as the thrust coefficient (i.e. $dC_{pow} = C_{pow,installed} - C_{pow,isolated}$), and presented on the right side of Figure 10. Here, the power coefficient of the installed configurations are similar to the isolated propeller for advance ratio's up to J = 0.3 in the experiments. After this, the power is reduced with increasing advance ratio. The results of the simulations show a power reduction that is linear with the advance ratio.

The results in Figure 10 show the steady loading information of the propeller, i.e. averaged over a full rotation. In reality, periodic variations in blade loading will be present as was shown by the inflow velocity contours of Figure 9. The waveform of the thrust at a given blade section (for example 0.75R) during a cycle can be compared for the different simulation techniques, and is presented in Figure 11 for J = 0.3 and J = 0.6.

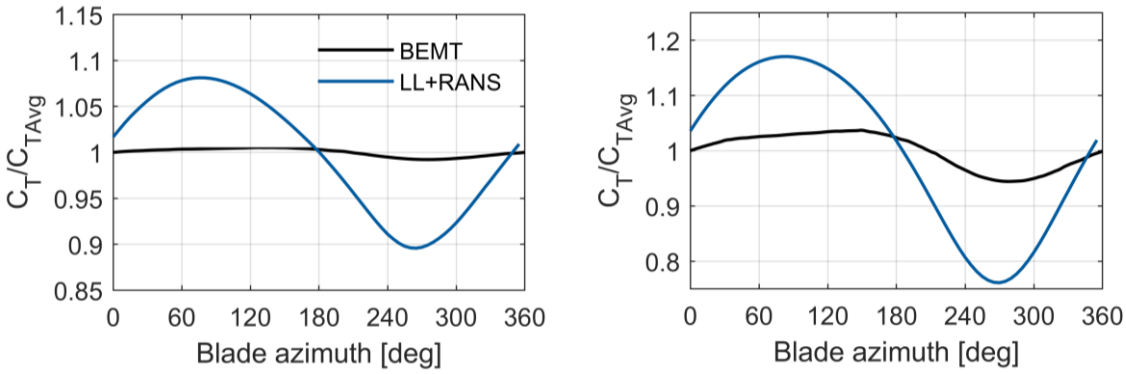

Figure 11 Blade sectional loading waveforms at 0.75R, normalized by the averaged thrust of the same blade section, for J = 0.3 (left) and J = 0 .6 (right).

Generally, the lifting-line formulation predicts an increasing degree of unsteady loading which is caused by the iterative coupling between propeller and wing-induced flow field. The contraction is limited in this way, which causes the propeller induced velocities to increase closer to the wing. This effect is not captured in the BEMT results, since it computes the loads of an isolated propeller in non-uniform inflow.

E. Propeller tonal noise trends

Tonal noise components are compared between the simulations and the experimental measurements. This is done for both measurements at the suction side of the wing, which investigate the noise source, and the measurements at the pressure side of the wing, able to show the potential of noise shielding. To minimize the effect of the broadband noise contributions, the experimental tonal noise is computed again by means of phased-locked Fourrier Transforms [18]. The results for the *dSPL* (i.e. $dSPL = SPL_{installed} - SPL_{isolated}$) of the first BPF for both the experiments and simulations can be found in Figure 12.

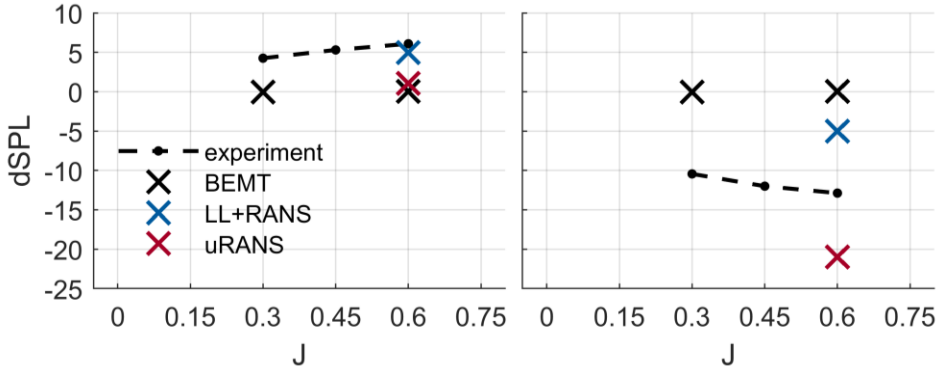

Figure 12 dSPL of the first BPF for the microphone on the suction side (left) and pressure side (right) in propeller disk plane as a function of the advance ratio *J*.

On the suction side of the wing, Figure 12 (left), an increase of the propeller noise is seen compared to the isolated case by a maximum of 6 dB for $J = 0.6$. This is well captured by the low-fidelity simulation using the iterative wing coupling (LL + RANS). The slight difference is likely caused by the presence of motor noise in the experiments. The BEMT formulation on the other hand show only minor difference in tonal noise compared to the isolated propeller. This indicates that the increase in noise is purely caused by the reflection and scattering surfaces of the wing, which are not taken into account in the BEMT formulation.

Towards the pressure side of the wing, at the right side of Figure 12, the experiments show a significant reduction of the BPF (13 dB) on the pressure side of the wing by shielding. This value is lower for the lifting line formulation, where a reduction of approximately 5 dB is found. Since the BEMT does not include the acoustic interaction between propeller and wing, the shielding characteristics are not captured and the noise on the wing's pressure side is strongly over predicted. The URANS results of Figure 12 (right) show a great amount of shielding. An impression of this results is shown in Figure 13, comparing the first BPF of the isolated and installed cases from the URANS results. The interference pattern due to the presence of the wing and the shielding on the lower side of the wing can be clearly seen from this.

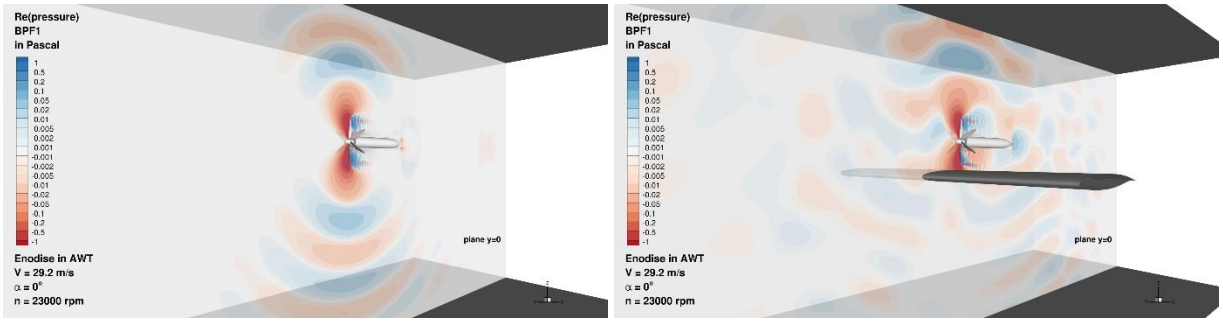

Figure 13 URANS result on medium grid: Real component of pressure Fourier transform at 1 BPF in a $z = 0$ plane through the propeller axis (left isolated; right installed).

VI. Conclusion

The tonal noise of an over-the-wing propeller has been investigated by means of experiments and three simulation techniques with increasing computational costs and propeller-wing coupling. The measurements show that the noise of the first BPF is reduced by up to 12 dB below the wing, by its shielding. However, at the suction side of the wing, the noise is increased by the reflection and scattering properties. The wing decreases both thrust and the power of the propeller by the increase in velocity compared to the free-stream. Additionally, this results in unsteady loading on the propeller blades, which causes the tonal noise of the propeller to be constant for reduced thrust. The simulations are able to capture the trends in propulsive and acoustic performance, but discrepancies are found when comparing to the measured results which requires additional research. Finally, the experiments indicate a strong contribution of broadband noise to the acoustic signature of the installed propeller, which should not be disregarded.

Acknowledgments

This research is funded by the European Union's Horizon 2020 research and innovation programme, under grant agreement No. 860103, project ENODISE (Enabling optimized disruptive airframe-propulsion integration concepts). The authors would also like to acknowledge Tim Deleij and Laurens de Haan for their assistance during the experiments. Additional gratitude is given to Tom Lanters for the design of the propeller mounting.

References

[1] Jansen, R., Bowman, C., Jankovsky, A., Dyson, R., & Felder, J. (2017). Overview of NASA electrified aircraft propulsion (EAP) research for large subsonic transports. *In 53rd AIAA/SAE/ASEE joint propulsion conference* (p. 4701).

[2] Borer, N. K., Patterson, M. D., Viken, J. K., Moore, M. D., Bevirt, J., Stoll, A. M., & Gibson, A. R. (2016). "Design and performance of the NASA SCEPTOR distributed electric propulsion flight demonstrator". In *16th AIAA Aviation Technology, Integration, and Operations Conference* (p. 3920).

[3] Kim, H. D., Perry, A. T., & Ansell, P. J. (2018, July). A review of distributed electric propulsion concepts for air vehicle technology. *In 2018 AIAA/IEEE Electric Aircraft Technologies Symposium (EATS)* (pp. 1-21). IEEE.

[4] Marcus, E. A., de Vries, R., Raju Kulkarni, A., & Veldhuis, L. L. (2018). Aerodynamic investigation of an over-the-wing propeller for distributed propulsion. *In 2018 AIAA Aerospace Sciences Meeting* (p. 2053).

[5] Broadbent, E. G. (1976). Noise shielding for aircraft. Progress in Aerospace Sciences, 17, 231-268.

[6] Müller, L., Heinze, W., Kožulović, D., Hepperle, M., & Radespiel, R. (2014). Aerodynamic installation effects of an over-the-wing propeller on a high-lift configuration. *Journal of Aircraft*, 51(1), 249-258.

[7] Veldhuis, L. L. M. (2005). Propeller wing aerodynamic interference.

[8] de Vries, R., & Vos, R. (2022). Aerodynamic Performance Benefits of Over-the-Wing Distributed Propulsion for Hybrid-Electric Transport Aircraft. *In AIAA SCITECH 2022 Forum (p. 0128).*

[9] Brouwer, H. H. (1992). On the use of the method of matched asymptotic expansions in propeller aerodynamics and acoustics. *J. Fluid Mech. 242*, (p. 117).

[10] Brouwer, H. H. (2010). Analytical method for the computation of the noise from a pusher propeller. AIAA Paper 2010-3848.

[11] Kok, J. C. (2009). A high-order low-dispersion symmetry-preserving finite-volume method for compressible flow on curvilinear grids. *Journal of Computational Physics*, 228, 6811-6832.

[12] van Arnhem, N., de Vries, R., Sinnige, T., Vos, R., Eitelberg, G., & Veldhuis, L. L. (2020). Engineering method to estimate the blade loading of propellers in nonuniform flow. *AIAA Journal*, 58(12), 5332-5346.

[13] Sears, W. R. (1941). Some aspects of non-stationary airfoil theory and its practical application. *Journal of the Aeronautical Sciences*, 8(3), 104-108.

[14] Hanson, D. B. (1983). Compressible helicoidal surface theory for propeller aerodynamics and noise. *AIAA Journal*, *21*(6), 881-889.

[15] Hanson, D. B. (1985). Noise of counter-rotation propellers. *Journal of Aircraft*, *22*(7), 609-617.

[16] Brooks, T., & Humphreys, Jr, W. (1999, May). Effect of directional array size on the measurement of airframe noise components. *In 5th AIAA/CEAS Aeroacoustics Conference and Exhibit* (p. 1958).

[17] Magliozzi, B., Hanson, D. B., & Amiet, R. K. (1991). Propeller and propfan noise. Aeroacoustics of flight vehicles: theory and practice, 1, 1-64.

[18] Rademaker, E., Sijtsma, P., & Tester, B. (2001). Mode detection with an optimised array in a model turbofan engine intake at varying shaft speeds. *In 7th AIAA/CEAS Aeroacoustics Conference and Exhibit* (p. 2181).